JOURNAL OF THERMOPHYSICS AND HEAT TRANSFER
Vol. 23, No. 3, July–September 2009

Stagnation-Region Heating Environment of the Galileo Probe

Chul Park*
Korea Advanced Institute of Science and Technology,
Daejeon 305-701, Republic of Korea

DOI: 10.2514/1.38712

The heating and ablating environment of the shock layer in the stagnation region of the Galileo probe is analyzed. Viscous shock-layer method is used assuming thermochemical equilibrium. Improvement is made to the existing methodology in calculating the equilibrium composition, radiation absorption in the vacuum ultraviolet wavelength range, and the effect of spallation. The calculated surface recession at the stagnation point agrees fairly closely with the flight data.

Nomenclature

B_λ = spectral intensity of the blackbody, $\mathrm{W/(cm^2 \cdot sr \cdot \mu m)}$
c = mass fraction of ablation-product gas
F_i = JANAF coefficients
f = Blasius-type nondimensional stream function
g = enthalpy normalized by freestream enthalpy
H = freestream enthalpy, J/kg
I = radiation intensity, $\mathrm{W/(cm^2 \cdot sr)}$
I_λ = spectral intensity, $\mathrm{W/(cm^2 \cdot sr \cdot \mu m)}$
$\dot{M}$ = thermochemical ablation rate, $\mathrm{g/(cm^2 \cdot s)}$
$\dot{m}$ = spallation rate, $\mathrm{g/(cm^2 \cdot s)}$
P = normalized rate of cooling by particulate sublimation, Eq. (2b)
Pr = Prandtl number
q_c = convective heat transfer rate, $\mathrm{W/(cm^2 \cdot s)}$
q_r = radiative heat transfer rate, $\mathrm{W/(cm^2 \cdot s)}$
R = normalized radiative heat addition, Eq. (2a)
Sc = Schmidt number for diffusion between the freestream and ablation-product gases
s = tangential coordinate, m
t = flight time, s
u = tangential velocity, m/s
y = distance from wall, cm
α = particle cloud extinction coefficient, Eq. (2)
ΔH = heat of ablation, J/g
ϵ_λ = spectral emission coefficient, $\mathrm{W/(cm^2 \cdot sr \cdot \mu m)}$
κ_λ = spectral absorption coefficient, $\mathrm{cm^{-1}}$
μ = viscosity, poise
ρ = density, $\mathrm{g/cm^3}$

Subscripts

p = particles
s = shock wave
t = turbulence
w = wall
0 = origin
∞ = freestream

Introduction

AN UNMANNED vehicle named the Galileo probe entered into the atmosphere of the planet Jupiter in 1995 [1]. Its forebody was thermally protected with a heat shield made of carbon-phenolic. Before the entry flight, the heating and ablation rates and the extent of recession of the heat-shield surface were predicted by Moss and Simmonds [2], among others. The calculation by Moss and Simmonds was made assuming the atmosphere of the planet to consist of a 89%H_2–11%He mixture.

The vehicle was equipped with a group of sensors named analog resistance ablation detectors (ARADs) to measure the surface recession. The progress of surface recession was successfully measured, and the information was transmitted to Earth. By analyzing the accelerometer record, the H_2-to-He mixture ratio was determined to be 86.4 to 13.6%. Theoretically, this heavier mixture should have produced heating and ablation rates higher than the 89–11 mixture considered by Moss and Simmonds [2].

Surprisingly, the extent of ablation at the stagnation region measured by ARAD 1 and 2 was found to be considerably smaller than predicted by Moss and Simmonds [2]. On the other hand, in the downstream region, the extent of ablation was larger than predicted. Recently, Matsuyama et al. [3] carried out the heating calculation for the 86–14 mixture. The calculated values for the downstream region were close to the flight data. However, in the stagnation region, the calculated values were still substantially higher than the flight data.

It is the purpose of the present work to examine this problem. Viscous shock-layer method is used instead of the computational fluid dynamics (CFD) approach commonly used, because it is free of the numerical singularity problem at the stagnation point.

For the Galileo probe vehicle, heating is mostly by radiation. Radiation emission from a hydrogen–helium mixture was studied experimentally in an electric-arc-driven shock tube by Leibowitz [4] before the Jovian entry. This experiment revealed that radiation emission behind a shock wave is not immediate, but occurs after a short time lag because of the time taken for dissociation, ionization, and electronic excitation (i.e., nonequilibrium relaxation phenomena). Howe [5] predicted that the radiative heating rate would be smaller than calculated by Moss and Simmonds [2] because of this phenomenon. In Fig. 1, the thickness of this radiationless region is shown for the Galileo probe entry conditions. As shown in the figure, the radiationless region is less than 1 mm. This is small compared with the shock-layer thickness for the probe, which was about 20 mm.

Furudate et al. [6] studied the nonequilibrium relaxation phenomenon in a hydrogen–helium mixture theoretically. They concluded that the nonequilibrium relaxation phenomenon played only a minor role in the Galileo entry.

For these reasons, equilibrium flow is assumed in the present work. The issues examined are the 1) accuracy of equilibrium state calculation, 2) vacuum ultraviolet absorption mechanisms, and 3) effect of spallation. The present work concludes that, unlike the

---

Presented as Paper 4109 at the 40th Thermophysics Conference, Seattle, WA; received 22 May 2008; revision received 15 October 2008; accepted for publication 15 October 2008.

*Visiting Professor, Department of Aerospace Engineering; cpark216@kaist.ac.kr. Fellow AIAA.

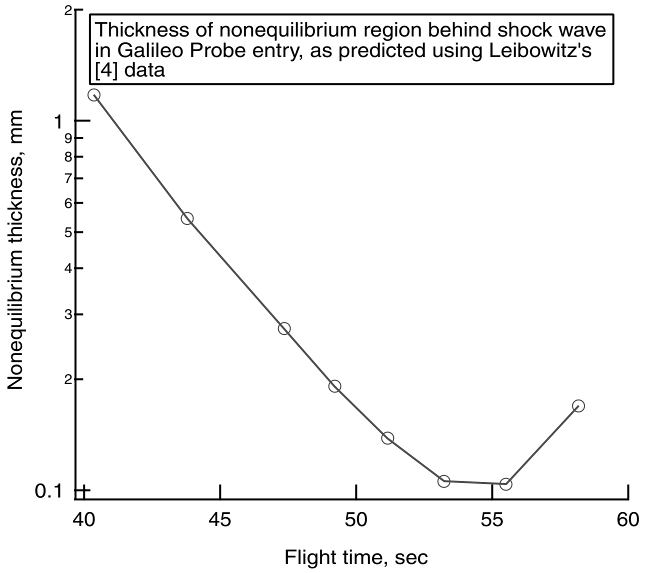

Fig. 1 Thickness of radiationless region behind normal shock in Galileo probe entry environment predicted by the work of Leibowitz [4] and Howe [5].

previous investigations, the calculated stagnation-region surface recession agrees with the flight data reasonably closely.

Method of Calculation

Flow Solution

Viscous Shock Layer Equations

The stagnation-region flowfield is solved using a viscous shock-layer method [7]. The condition immediately behind the normal shock wave is calculated using the Rankine–Hugoniot conditions. The mass and momentum of the flow is represented by a Blasius-type nondimensional momentum variable f. In the stagnation region, the f equation is a third-order nonlinear ordinary differential equation and is well known [7]. It is simplified by neglecting the pressure variation in the normal direction and is linearized in the present work in the form

$$\left(\frac{\rho\mu}{\rho_s\mu_s}f''\right)' + f_1 f'' + \frac{1}{2}\left(2\frac{\rho_\infty}{\rho} - f_1' f'\right) = 0 \tag{1}$$

Here, the prime denotes differentiation by a normalized tangential distance [7]. The quantities f_1 and f_1' are the assumed values of f and f': they are replaced by f and f' after solving Eq. (1). The outer boundary condition (i.e., the Rankine–Hugoniot condition) specifies that f would attain a prescribed value and f' would be unity at the shock wave. At the wall, the ablation rate specifies the value of f. The quantity f' is zero at the wall. Initially, f_1, f_1', ρ/ρ_s, and μ/μ_s are assumed, and integration is performed to satisfy these boundary conditions.

The energy of the flow is represented by a nondimensional energy function g. It satisfies a linear ordinary differential equation:

$$\left(\frac{1}{Pr}\frac{\rho\mu}{\rho_s\mu_s}g'\right)' + fg' + R - P = 0 \tag{2}$$

Here, R and P are

$$R = \frac{\dot{R}}{2(du_s/ds)H} \tag{2a}$$

$$P = \frac{\dot{P}}{2(du_s/ds)H} \tag{2b}$$

and $\dot{R}$ and $\dot{P}$ are the radiative power gain per unit volume and the power loss per unit volume due to the cooling in vaporizing the particles, respectively. Equation (2) assumes that the Lewis number is unity.

The flow is assumed to be in thermochemical equilibrium, as mentioned. To obtain the updated values of the ratio $\rho\mu/\rho_s\mu_s$ appearing in Eqs. (1) and (2) and ρ_∞/ρ appearing in Eq. (1), one must calculate the equilibrium thermodynamic state. To do so, one must know the ratio of the elemental mass fractions. Following the common practice, this is obtained by assuming that the ablation-product gas and the freestream gas diffuse through each other. The diffusion equation is written for the mass fraction of the ablation-product gas mass fraction c in the form

$$\left(\frac{1}{Sc}\frac{\rho\mu}{\rho_s\mu_s}c'\right)' + fc' = 0 \tag{3}$$

To be precise, vaporization of the spalled particles produces a gaseous ablation product, and this must be accounted for in Eq. (3) as an additional term. However, this procedure encounters a difficulty: the vaporization phenomenon not only changes the elemental mass fraction c, but also produces displacement and hence a change in the flowfield. To circumvent the problem, all spalled particles are assumed to penetrate the shock layer and reach the freestream; in the freestream, the particles are vaporized by the hypersonic impacts of the oncoming flow. With this simplification, one needs only to specify the shock value of c to account for the presence of the ablation product in the freestream.

The value c is unity at the wall. At the shock, with the simplification made, c takes the value equal to the ratio of the rate of the spalled particles penetrating the shock layer to the freestream mass flow rate.

From the solution of the c equation and the solution of the g equation, the equilibrium state is calculated. Using the equilibrium state parameters, $\rho\mu/\rho_s\mu_s$ and ρ/ρ_s are calculated. Using these, Eq. (1) is solved to obtain its next-level approximation. This procedure is repeated until the f, g, and c functions reach constant values.

Turbulence

The flow in the stagnation region is laminar unless there is ablation. The ablation product is turbulent at the wall according to the injection-induced turbulence theory [8]. According to this theory, the turbulence eddy viscosity at the wall due to ablation is up to 14 times the laminar value for the Galileo probe. But this turbulence decays in the boundary layer. In [3], this effect was accounted for, showing that this phenomenon does not affect the flowfield substantially. For this reason, most of the present calculation was performed assuming the flow to be laminar. Viscosity is calculated using the well-known Wilke's mixture rule employing the available collision integrals.

However, the injection-induced turbulence theory does not account for the presence of spalled particles. The relative motion between a solid particle and the surrounding flow is very likely to produce turbulence. Unfortunately, there is no way to know the strength of this particle-induced turbulence.

To explore the possible effect of this particle-induced turbulence, turbulent calculation was performed in the present work for one selected case. Because the spalled particles exist throughout the shock layer, as will be shown later, the effective viscosity (i.e., the sum of the molecular and turbulent viscosities) is assumed to be a constant multiple of the laminar viscosity. The Prandtl number and Schmidt number are both assumed to be 0.7 for both laminar and turbulent calculations. This is consistent with the assumption of a unity Lewis number.

Shock Standoff Distance

The present viscous shock-layer method is a fairly loose approximation in treating momentum, in that it assumes pressure to be constant across the shock layer. As a result, the method tends to consistently undercalculate the shock standoff distance. To produce the same shock standoff distance as that obtained in [3], the nose radius was taken to be 28.8 cm (i.e., a factor of 1.2 was multiplied to the actual nose radius of 24 cm). This procedure undercalculates the convective heat transfer rate by about 10%. Fortunately, the convective heat transfer rate is negligibly small in this environment, and therefore this error would be inconsequential. Such a loose approximation is justified here, because the problems the present work seeks to solve (i.e., thermochemistry, radiation, and spallation) are unaffected by the looseness of the momentum treatment.

Equilibrium Composition

Eight chemical species are assumed to exist: He, H_2, H, H^+, C, C_2, C_3, and C^+. Equilibrium thermodynamic properties are calculated using the well-known Gibbs free-energy-minimizing technique. In calculating the species thermodynamic properties, the JANAF curve fit [9] was used. In this curve-fit method, thermodynamic variables are expressed using six parameters F_i ($i = 1$ to 6). Two sets of these six parameters are given in the original work [9]: one for the temperature range from 500 to 3000 K and one from 3000 to 6000 K. The original JANAF coefficients for H and H^+ for the 3000 to 6000 K range, taken from [9], are given in Table 1. The set for 3000 to 6000 K was used with modification. The modification was made so that the calculated temperature and H^+ concentration agree with the values obtained using partition functions at the point immediately behind the normal shock wave.

The partition functions are calculated by accounting for all H-atom levels up to one level just below truncation by the charge-shielding phenomenon. Modification was made for F_2 for H and F_1 for H^+. F_2 for H represents the electronic excitation energy, which is inaccurate in the original JANAF coefficient tables, because only five energy levels are accounted for. F_1 for H^+ represents the ionization potential of H, which is inaccurate in the original JANAF coefficient tables, because the lowering of ionization potential is not accounted for. These modified values of H and H^+ JANAF coefficients are presented in Table 2. These modified parameters result in H^+ concentration and temperature that agree to four significant figures with those determined using the partition function method behind the normal shock. In the interior of the inviscid region and in the boundary layer, this method results in slightly erroneous temperatures and H^+ concentrations. But in these low-temperature regions, radiation is weak and so the error is inconsequential.

Radiation

Radiation calculation was carried out using 10,001 wavelength points spread between 400 and 24,000 A at equal energy intervals.

Table 1 Original JANAF coefficients for H and H^+ in the temperature range from 3000 to 6000 K given in [9]

For H	For H^+
$F_1 = 5.20997e4$	$F_1 = 3.67182e5$
$F_2 = 1.34229e4$	$F_2 = 1.34229e4$
$F_3 = 4.96794e0$	$F_3 = 4.96799e0$
$F_4 = 9.21055e-9$	$F_4 = 0.00000e0$
$F_5 = 2.32451e2$	$F_5 = 2.16503e-1$
$F_6 = 3.88627e1$	$F_6 = 3.74820e1$

Table 2 F_2 for H and F_1 for H^+ used in the present work

Time	F_2 for H	F_1 for H
40.35	3.34900e4	3.65140e5
43.79	3.37000e4	3.64500e5
47.36	3.32740e4	3.63500e5
49.21	4.43200e4	3.41830e5
51.16	4.08160e4	3.38700e5
53.23	3.52570e4	3.34800e5
55.52	2.79700e4	3.31800e5
58.19	2.19659e4	3.58680e5

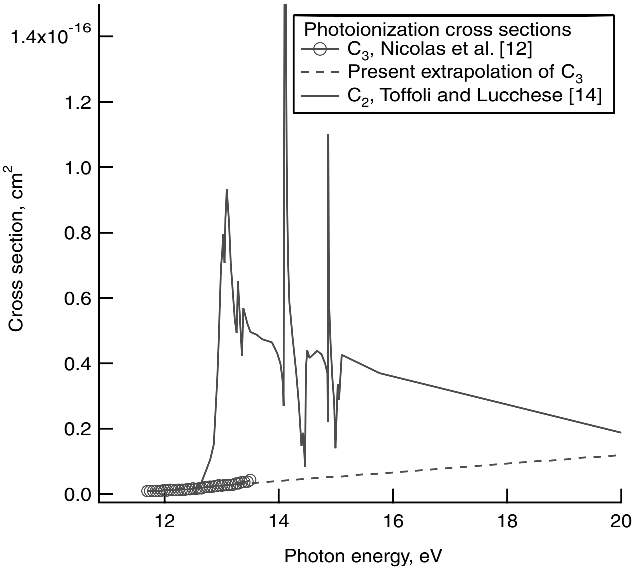

Fig. 2 Photoionization cross sections of C_3 and C_2.

The line radiation, the bound–free continuum, and the free–free continuum radiation from H are well known, and have been used in [2,3]. The same method was used for the present work. In addition, the line radiation from the 20 strongest lines [10] and the bound–free continuum [11] for C are accounted for. The uniform slab approximation is made in radiative transfer calculation. For comparison purposes, calculation was also made accounting for the spherical nature of the shock layer for the peak-heating point.

Radiation absorption in the ablation-product layer occurs mainly from C_3 and C_2. For C_3, the Swings band and the vacuum ultraviolet absorption band in the wavelength range from 120 to 180 nm are also well known and were used in [2,3]. These are used here also.

In addition, there are photoionization continua for both C_3 and C_2 in the wavelength range below 110 nm that have not been accounted for in [2,3]. Nicolas et al. [12] measured the absorption rate of C_3 in a laser ablation experiment at an unknown low temperature. The published article does not give the absolute values of the absorption cross section. However, one of the authors provided the original data. The absolute cross section was determined from the original data to within an uncertainty factor of about 2 with his help.

Photodissociation and ionization continuum of C_2 was calculated by Pouilly et al. [13] and by Toffoli and Lucchese [14] at a low temperature. The two sets of data agree reasonably well. In the present work, the data by Toffoli and Lucchese are adopted. In Fig. 2, the photoionization cross sections of C_3, the present extrapolation thereof, and those for C_2 used in the present work are presented.

The cross-sectional values are stretched for use at high temperatures. In a photoionization process, the electronic transition moment is nearly independent of vibrational and rotational levels. But, at high temperatures, the upper vibrational and rotational states are populated, whereas the ground state is thinned. This shifts the photoionization threshold to a lower photon energy (i.e., to a longer wavelength), according to the Boltzmann distribution rule.

A similar spreading is performed for the vacuum ultraviolet band of C_3 in the 120 to 180 nm range. This band, in reality, consists of bound–bound transitions. Assuming that electronic transition moment does not vary with vibration or rotational levels, the band spills out into longer and shorter wavelengths as high vibrational and rotational levels are excited. This phenomenon can also be accounted for by applying the Boltzmann distribution rule. Resulting absorption cross sections for C_3 in the short wavelength range are presented in Fig. 3.

For C_2 in the visible wavelength range, the Swan band is the strongest. This band is accounted for in the present work. Its absorption spectrum is calculated using a line-by-line method with 200,001 wavelength points in the wavelength range from 3360 to 7600 A. The resulting absorption cross section is smoothed.

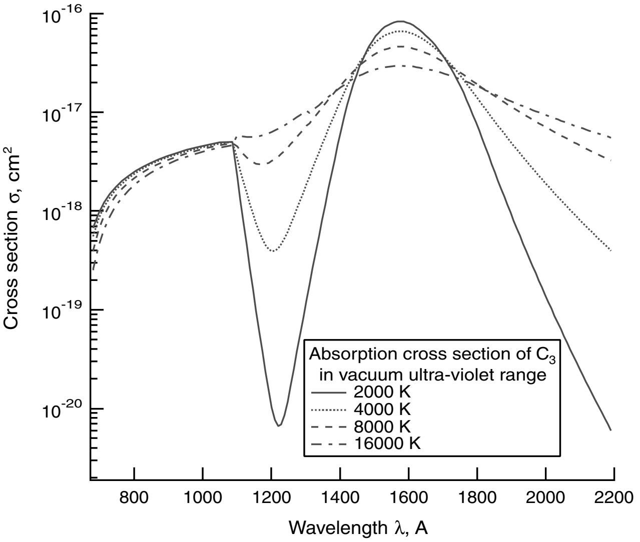

Fig. 3 Absorption cross section of C_3 in the vacuum ultraviolet wavelength range.

For C_2, there are eight known band transitions in the wavelength range from 1000 to 1800 A (i.e., $f^3\Sigma_g^-$-$a^3\Pi_u$, $g^3\Delta_g$-$a^3\Pi_u$, $F^1\Pi_u$-$X^1\Sigma_g^+$, $4^3\Sigma_g^-$-$a^3\Pi_u$, $3^1\Pi_u$-$X^1\Sigma_g^+$, $j^3\Delta_g$-$a^3\Pi_u$, $h^3\Sigma_g^-$-a3PIu, and $k^3\Sigma_g^+$-$a^3\Pi_u$). Bruna and Grein [15] provided band strength factors to four of these eight bands (i.e., those for the f-a, g-a, F-X, and 3P-X transitions). For the rest, the strength factor is assumed to be the same as those for the resembling transitions. Line-by-line calculation was performed for these eight bands, and the resulting cross sections are smoothed. The resulting cross sections for C_2 in the vacuum ultraviolet wavelength range are presented in Fig. 4.

The well-known radiative transfer equation is integrated numerically along 9 directions separated by 10 deg intervals along the stagnation streamline to obtain the intensities in those directions. Radiative flux is evaluated by numerically integrating these intensity values over the 2π solid angle. A cubic integration routine is used for this purpose to ensure sufficiently high fidelity.

Spallation

The spallation phenomenon for the Galileo probe was first studied both theoretically and experimentally in [16]. In that study, the spalled particles were assumed to be spherical in shape, and their trajectories were calculated for three different initial sizes (5, 100, and 300 μm) for the flow environment of the Galileo probe. All particles were assumed to be ejected from the wall normally. The 100 and 300 μm particles did not vaporize totally within the shock layer. The 5 μm particles typically disappeared within a distance of 10 mm away from the ablating wall.

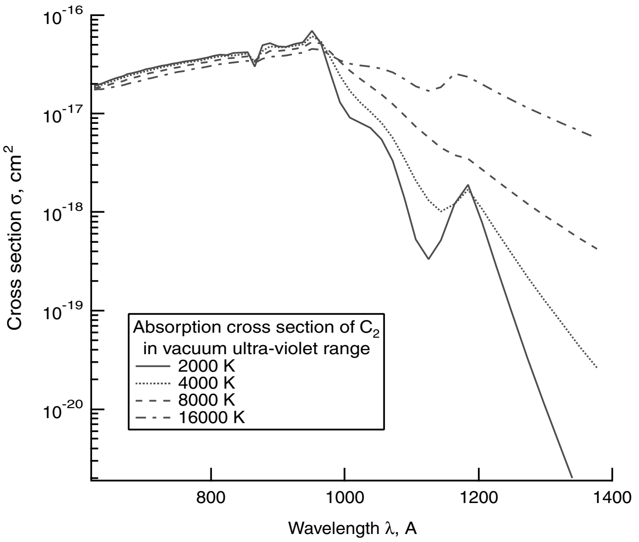

Fig. 4 Absorption cross section of C_2 in the vacuum ultraviolet wavelength range.

Experimentally, the motion pictures taken of the spallation phenomena were analyzed to determine the speed of the spalled particles [16]. For the particles visible in the pictures, the fastest particles were observed at very high radiative heating rates (heating rates higher than 50 $\mathrm{kW/cm^2}$) to move at about 300 m/s. The slowest particles, observed at the lowest tested heating rates, moved at about 25 m/s. In the range of heating rates of 20 to 30 $\mathrm{kW/cm^2}$, the particles seemed to move typically at about 100 m/s.

In [17], the theoretical model in [16] was extended by introducing size and ejection velocity distribution functions. Both size and velocity distribution functions are characterized by their median values and exponents over the (size or velocity) variables. The calculation was made for Stardust's Earth entry conditions.

Park et al. [18] measured the extent of radiation attenuation by the cloud of spalled particles in the shock layer for the phenol-impregnated carbon ablator (PICA) used for the Stardust vehicle. Radiation intensity I attenuates in a cloud of particles by the Beer's law:

$$\frac{I}{I_0} = \exp(-\alpha y) \tag{4}$$

The coefficient α is known as the extinction coefficient. It is the sum of cross-sectional areas of all particles contained in a unit volume, e.g., 1 $\mathrm{cm^3}$. When the heat transfer rate was about 1.6 $\mathrm{kW/cm^2}$, the extinction coefficient of the particle cloud was about 0.11 $\mathrm{cm^{-1}}$ near the wall in the experiment by Park et al. [18]. The spallation rate to produce this extinction coefficient was calculated in that work to be of the order of 10^{-3} $\mathrm{g/(cm^2 \cdot s)}$. The measured extinction coefficient values were plotted against the distance from the wall. Four independent such plots were obtained in the experiment. Five parameters (the median size, median velocity, frequency-size exponent, frequency-velocity exponent, and spallation rate) that best reproduce the four extinction coefficient plots were determined, as follows.

Particle trajectory calculation was performed for 59 representative diameters, accounting for collisional heating, gas irradiation, surface radiation, and vaporization, as in [17]. The aforementioned five parameters were varied in each calculation. The parameters that best reproduced the measured extinction coefficient variation were derived. The results showed that the assumption that all particles are ejected with a same speed is satisfactory. The exponent on size in describing the size distribution was found to be −0.65. The median diameter was deduced to be 10 μm. The ejection speed that best reproduced the extinction data varied from 12.4 to 35.1 m/s, corresponding to the heating rates of 410 and 1710 $\mathrm{W/cm^2}$.

The spallation behavior of the carbon-phenolic material used for the Galileo probe vehicle was studied by Lundell [19]. A laser beam was directed toward an ablator sample, and the particles ejected from the surface were collected and weighed. For the material used for the stagnation region of the heat shield (chop-molded carbon-phenolic), spallation was observed when the radiative heat flux incident on the wall, q_{rw}, exceeded 14.5 $\mathrm{kW/cm^2}$. Above this heat flux, the spallation rate was found to be describable by

$$\dot{m} = 990 \times (q_{rw} - 14.5)\ \mathrm{kg/(m^2 \cdot s)} \tag{5}$$

where q_{rw} is in $\mathrm{kW/cm^2}$. Note that the threshold q_{rw} of 14.5 $\mathrm{kW/cm^2}$ was exceeded during the peak-heating period in the entry trajectory of the Galileo probe.

In Lundell's [19] experiment, the extinction coefficient was not determined consciously. Presently, however, one can deduce the order of magnitude value of extinction coefficient from the result of the experiment. In his experiment, he saw that the particle cloud attenuated the laser radiation significantly [19]. He had to blow off the particle cloud using a tangentially directed gas jet: the ablation rate was found to increase significantly when the blowing was applied [19]. (The present author witnessed the experiment.) This significant radiation attenuation is interpreted here to mean a 30% reduction in radiation intensity. The ablating target he used seemed to produce a particle cloud of a thickness of the order of 3 mm. For the material used for the stagnation region, his experiment produced spallation rates between 0.061 and 0.174 $\mathrm{g/(cm^2 \cdot s)}$, a representative value being 0.1 $\mathrm{g/(cm^2 \cdot s)}$ [19]. By Eq. (2), a 30% reduction in 3 mm represents an attenuation of $1/e = 0.368$ for a cloud thickness of 10 mm. This leads to a calibration point stating that a spallation rate of 0.1 $\mathrm{g/(cm^2 \cdot s)}$ produces an extinction coefficient of 1 $\mathrm{cm^{-1}}$.

This calibration constant for extinction coefficient is the value of extinction coefficient in the volume adjacent to the ablating wall. Because the particles shrink in size as they travel away from the wall, the extinction coefficient decreases with distance. By calculating the trajectories of the particles as was done in [16–18], one can determine the spatial distribution of the extinction coefficient. To do so, the median diameter (10 μm) and the size-frequency exponent (-0.65) were assumed to be the same as for PICA. The particle ejection speed was assumed to be 100 m/s, the median value obtained in [16].

The result of such calculation is shown for the peak-heating point in Fig. 5 by the dashed curve and is compared with the experimental data for Stardust obtained in an arc-jet wind-tunnel experiment that closest resembles the Galileo case. The figure shows that particles disappear faster in the Stardust environment, despite the fact that the shock-layer pressure was lower for the Stardust. This can be attributed to the presence of atomic oxygen in the Stardust case: the oxygen atoms bombarding the particles quickly oxidize solid carbon. The calculated shape of extinction coefficient variation implies that half or more of the particles, for which the median diameter is assumed to be 10 μm, disappear within the distance of 2 cm. According to [16], 5-μm-diam particles disappear typically in 1 cm. Thus, Fig. 5 is compatible with the findings in [16]. Figure 5 is also compatible with the experimental data in [18] when one accounts for the presence of oxygen atoms in the experiment.

Carrying out the particle trajectory calculation inside the flowfield calculation was met with a difficulty: the flow solution did not converge. To avoid this difficulty, a straight-line distribution of extinction coefficient is assumed, as shown by the solid line in Fig. 5. The base of the solid line is the value deduced from Eq. (5) and the calibrated extinction coefficient value corresponding to the base value. The slope of the solid line is the slope at the boundary-layer edge. This linear approximation gave a satisfactory convergence of the flow calculation. From the extinction coefficient distribution, the blockage of radiative flux toward the wall is calculated as follows.

When the extinction coefficient of the particle cloud is given as α, the effective spectral emission coefficient $\bar{\epsilon}_\lambda$ and the effective spectral absorption coefficient $\bar{\kappa}_\lambda$ become

$$\bar{\epsilon}_\lambda = (1-\alpha)\epsilon_\lambda + \alpha B_\lambda(T_p) \tag{6}$$

$$\bar{\kappa}_\lambda = (1-\alpha)\kappa_\lambda + \alpha \tag{7}$$

where ϵ_λ and κ_λ are the emission and absorption coefficients in the absence of particles.

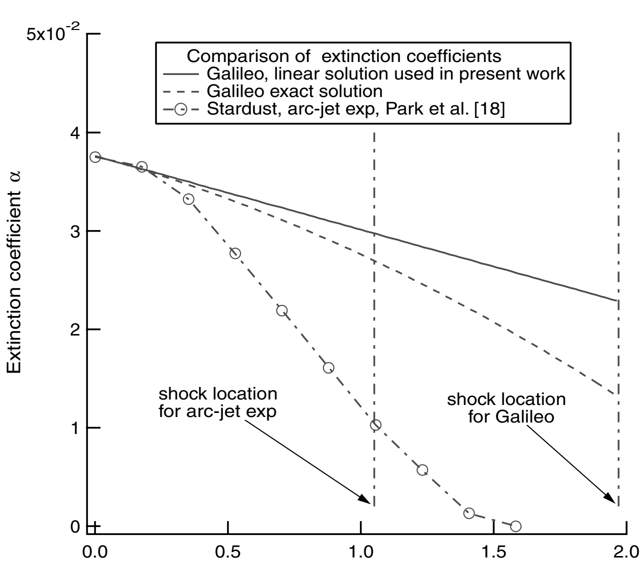

Fig. 5 Extinction coefficient distribution at 53 s point.

The linear approximation overestimates the blockage of radiation in the region near the shock wave. However, this error is not large, because the wall-ward radiative flux is small near the shock wave, as will be shown later.

Wall Conditions

The carbon-phenolic used for the heat shield contains small amounts of hydrogen and oxygen. These are ignored, and the material is assumed to be pure carbon. The wall temperature is the same as that used in [2,3]. The steady-state ablation assumption introduced in [2] is used also: that is,

$$q_{rw} + q_c - 5.679 \times 10^{-5} T_w^4 = \dot{M}\Delta H \tag{8}$$

The heat of ablation ΔH is calculated using the heat of formation value of -372 J/g determined experimentally by Wakefield and Pitts [20]. Over the range of temperature from 3700 to 4100 K, the heat of ablation is expressible approximately as

$$\Delta H = 23,307 - 0.825(T_w - 4000)\ \mathrm{J/g}$$

The thermochemical ablation rate $\dot{M}$ and the spallation rate $\dot{m}$ that satisfy the spallation Eq. (4) and the steady-state ablation condition (8) are obtained through trial and error.

Results

General Features of Solutions

Compared with the uniform slab, the radiation calculation made at the peak-heating point accounting for the spherical nature of the shock layer showed radiation flux less than 1% (0.81 to 0.98%) lower. This difference is ignored in the present work.

In Fig. 6, convergence patterns of the shock standoff distance and the wall radiative heat flux are shown. The calculated case is that given by Matsuyama et al. [3]. The figure compares the calculated values with the corresponding values obtained by Matsuyama et al.

In the calculation, the first 14 iterations were made without radiation. Between the 15th and 20th iterations, only 10% of the calculated radiative power change is accounted for. As shown in this figure, a converged solution is obtained after about 40 iterations. The averages of the 36th to the 45th values are used as the converged values. As shown in the figure, the shock standoff distance calculated in the present work closely matches the value obtained by

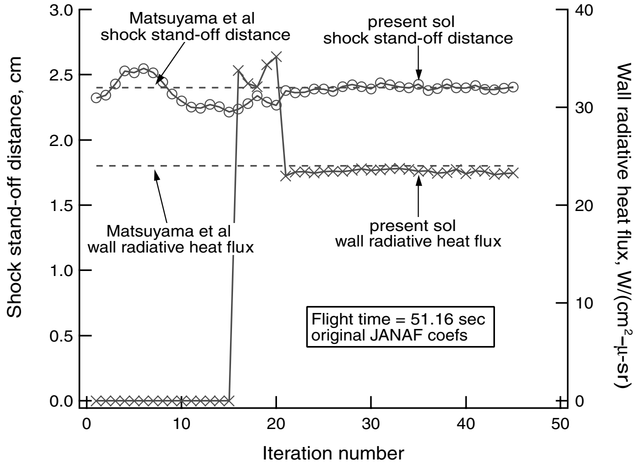

Fig. 6 Convergence pattern of the shock standoff distance and wall radiative heat flux, and comparison with the values by Matsuyama et al. [3].

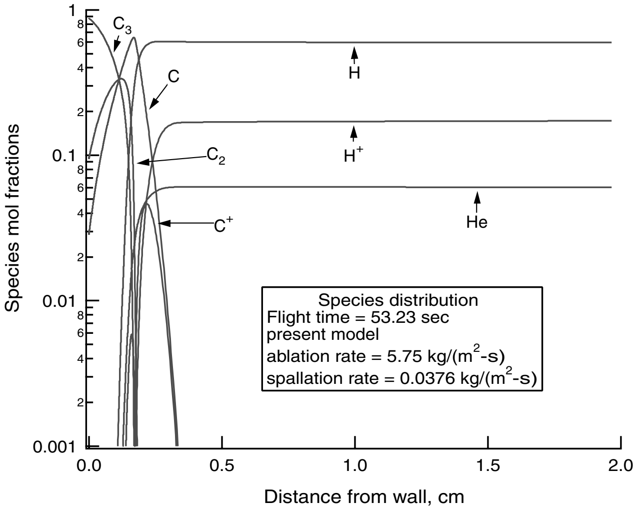

Fig. 7 Species mol fractions in the shock layer for the peak-heating point.

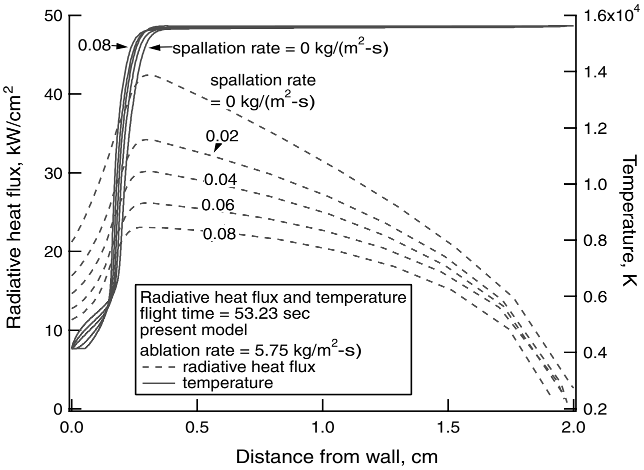

Fig. 8 Temperature and radiative heat flux directed toward wall for different spallation rates.

Matsuyama et al. [3]. As mentioned, this agreement is obtained in the present work by assuming the nose radius to be 1.2 times the true value.

In Fig. 7, species mole fraction distribution is shown for the peak-heating point, $t = 53.23$ s. As shown, the inviscid region of the shock layer contains H, H$^+$, and He. In the ablation layer, C_3 and C_2 are the main constituents.

In Fig. 8, temperature distribution and the distribution of radiative heat flux directed toward the wall are shown for the peak-heating point for different spallation rates. One sees that radiative heat flux reaches the peak at the edge of boundary layer and falls to roughly half its value at the wall. Radiative heat flux decreases as spallation rate increases. This is because the particles block radiation [see Eqs. (6) and (7)]. Temperature is also affected by spallation. Near the wall, temperature change is evident. In the inviscid region, there is a slight decrease in temperature with increase in spallation rate. This is due to the cooling effect of the particles [see Eq. (2)]. Near the shock wave, the radiative heat flux is relatively small. The linear approximation of extinction coefficient variation shown in Fig. 5 will make a relatively small error for this reason.

In Fig. 9, the radiation spectrum is shown at the boundary-layer edge and wall for the peak-heating point. The absorbing bands are indicated in the figure. The wavelength range marked as *absorption by extended vacuum ultraviolet (VUV)* is the range in which the newly added vacuum ultraviolet absorption bands are active. As shown, the new VUV bands are very effective in absorbing radiation.

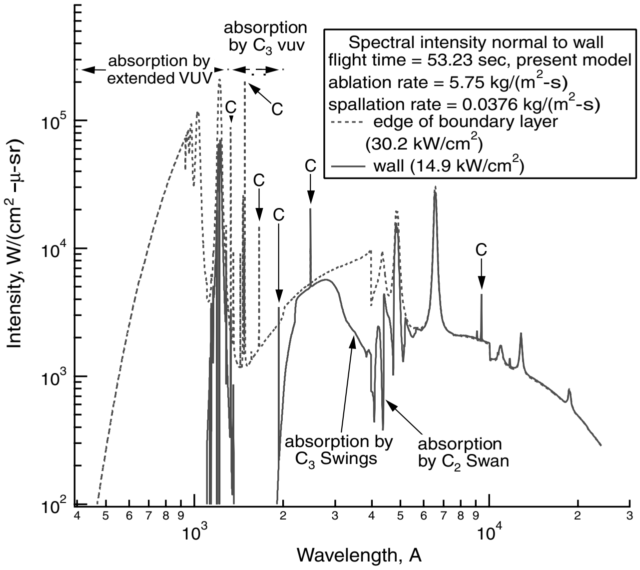

Fig. 9 Spectral intensity normal to wall for the peak-heating point.

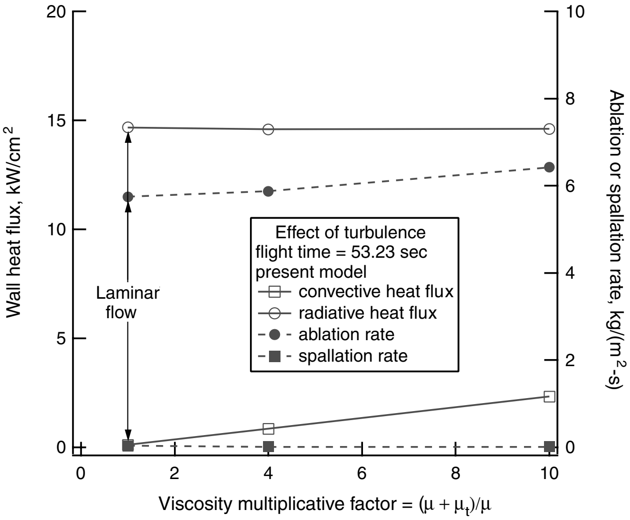

Fig. 10 Effect of increased effective viscosity on heating and ablation rates.

In Fig. 10, the effect of turbulence is shown. Here, the viscosity value of the laminar flow is increased by a factor of 4 and 10 throughout the flowfield. As mentioned earlier, this turbulence is considered to be due to the relative motion of the particles: the turbulence produced by the gaseous ablation decays in the boundary layer. As the figure shows, the wall heat transfer rate and spallation rate are affected very little. However, the ablation rate is increased slightly. The increase in convective heating rate is substantial when the multiplicative factor is 10.

In Table 3, comparison is made between the present solutions and the solution by Moss and Simmonds [2] and that by Matsuyama et al.

Table 3 Comparison between the present results and the results by Moss and Simmonds [2] and by Matsuyama et al. [3]

Case	$\dot{M}$ kg/(m$^2\cdot$s)	q_{rw} kW/cm^2
89%H$_2$–11%He, 310 kg, 51.5 s (alt = 131.6 km)		
Moss and Simmonds [2]	8.2	25.6
Present work	9.23	22.9
89%H$_2$-13.6% He, 51.16 s (alt = 130 km)		
Matsuyama et al. [3]	10.0	24.6
Present work	9.49	23.4

Table 4 Steady-state solutions for Galileo probe at the stagnation point obtained using the present model [3]

Flight time, s	Altitude, km	Ablation rate, $kg/m^2 \cdot s$	Spallation rate $kg/m^2 \cdot s$	q_r boundary-layer edge kW/cm^2	q_r wall kW/cm^2	q_c wall kW/cm^2
40.35	190	0.473	0	3.713	2.031	0.4179
43.79	170	1.128	0	8.369	3.707	0.2283
47.36	150	2.943	0	19.42	8.120	0.1562
49.21	140	4.459	0	28.34	11.75	0.1537
51.16	130	5.672	0.0120	34.38	14.68	0.1375
53.23	120	5.749	0.0376	30.18	14.88	0.1151
55.52	110	5.664	0.0174	25.01	14.68	0.1568
58.19	100	1.604	0	5.310	4.743	0.7707

[3]. As the table shows, the present method reproduces those earlier results reasonably closely.

Heating, Ablation, and Recession

Table 4 presents the steady-state solution for the Galileo probe at the stagnation point.

In Fig. 11, the stagnation-point heating rates are shown at each trajectory point. The four different methods mentioned earlier are compared here:

1) The calculation made with the original JANAF coefficients, the original VUV absorption mechanisms, and without spallation.

2) The calculation made with the modified JANAF coefficients, the original VUV absorption mechanisms, and without spallation.

3) The calculation made with the modified JANAF coefficients, extended VUV absorption mechanisms, and without spallation.

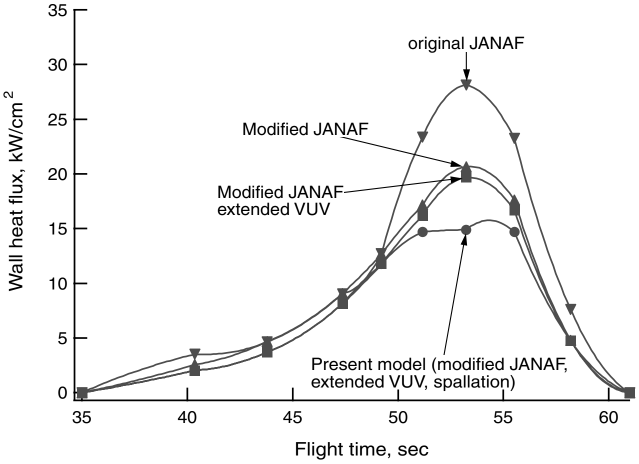

Fig. 11 Wall heating rates at each trajectory point.

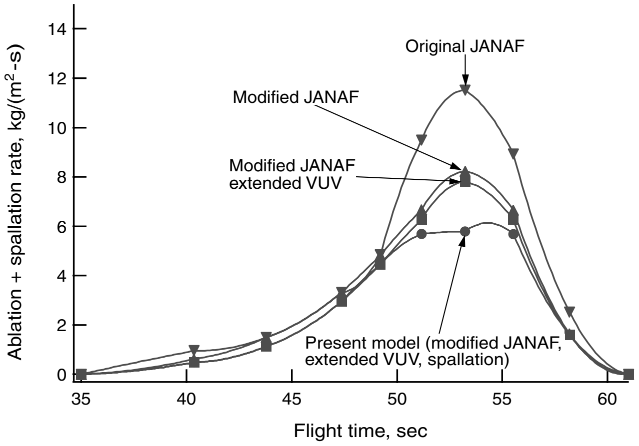

Fig. 12 Ablation and spallation rate at each trajectory point, calculated by four different methods.

4) The present model which uses the modified JANAF coefficients, extended VUV absorption mechanisms, and with spallation.

As shown, the present method gives the smallest heating rates. When the spallation phenomenon is not included, heating rates are larger. When the extended VUV absorption is excluded, heating rates become still larger. When the original JANAF coefficients are used, the heating rates are the largest.

In Fig. 12, the steady-state ablation rate and spallation rate are shown at all trajectory points for four different calculations. The curves joining the calculated points are obtained through a second-order interpolation. The ablation rates behave as the heating rates, as expected.

By integrating the curves in Fig. 12, surface recession is obtained. In Fig. 13, the results are shown for the four calculations and compared with the flight data. As shown, the present model closely reproduces the flight data. Matsuyama et al.'s [3] value falls between the highest two calculations made here.

Discussion

The foregoing results show that there are three reasons why the previous investigators overpredicted the surface recessions at the stagnation point: inaccurate thermochemical state calculation, inadequate accounting of VUV absorption, and neglecting of spallation. When these three items are corrected, the calculated surface recession agrees with the flight data. It is especially noteworthy that spalled particles function efficiently as a radiation blocker. When the wall heating rate exceeds the spallation threshold, spallation sets in. As a result, the wall heating rate cannot be much larger than the threshold heating rate.

The present finding will have considerable implications on the heating-ablating analysis of the downstream region. The heat-shield material used in the downstream region (tape-wrapped carbon-phenolic) was different from that used for the stagnation region. The downstream material was found by Lundell [19] to start spallation at 8.5 kW/cm^2, instead of 14.5 kW/cm^2 for the stagnation region. This means that the shock layer in the downstream region contained

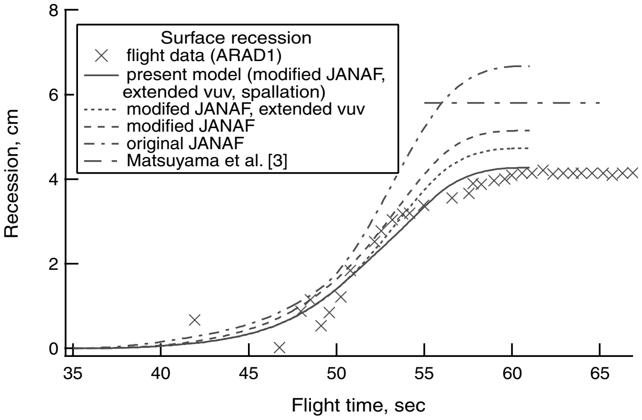

Fig. 13 Progression of surface recession compared among different methods.

much more spalled particles than the stagnation region. Radiative heat flux reaching the wall must have been reduced to values slightly larger than the threshold of 8.5 $\mathrm{kW/cm^2}$.

What other effect the spalled particles will have on the heating rates in the downstream region is not known at this time. Because the solid particles released in the upstream region will naturally flow downstream, the downstream region will be rich with solid particles. This may cause strong turbulence in the downstream region. According to Fig. 11, the convective heating rate becomes respectable when turbulence is strong. Radiation by carbon may also become substantial. The heat trapped by the spalled particles flows downstream and is bound to contribute to increasing the convective heating rate there.

The present calibration procedure for determining the extinction coefficient for a given spallation rate (see the Spallation section) is crude. But accuracy of this calibration constant is not so important for the following reason: when the radiative heat flux reaching the wall exceeds 14.5 $\mathrm{kW/cm^2}$ [see Eq. (5)], the spalled particles produce a radiation shield and so the radiative heat flux reaching the wall is prevented from rising much further. The wall radiative heat flux value can reach values only slightly above 14.5 $\mathrm{kW/cm^2}$, as shown in Table 4. In the present calculation, for the 53 s point, this excess heat flux is $14.88 - 14.5 = 0.38\ \mathrm{kW/cm^2}$. The calibration constant affects this excess value inversely. For instance, if the calibration constant is twice the value used in the present work, the excess heat flux will be $0.38/2 = 0.19\ \mathrm{kW/cm^2}$, resulting in the wall heat flux value of $14.5 + 0.19 = 14.69\ \mathrm{kW/cm^2}$, which is only a small difference from 14.88 $\mathrm{kW/cm^2}$. Consequently, the ablation rate, which is proportional to the wall heat flux value (spallation rate is a negligibly small portion of the ablation rate), is also insensitive to the accuracy of the calibration constant.

To a minor extent, the VUV absorption values used in the present work is uncertain. As mentioned, there are 8 molecular bands in the wavelength range from about 1000 to 2000 A. Intensity is known only for four of them. Even for these four, the accuracy of the intensity parameter is uncertain. As mentioned, for C_3, photoionization cross section is uncertain by a factor of 2. Improvement can be made on these. When radiation is absorbed in the boundary layer, the local temperature is raised. This hot gas will flow downstream and contribute to increasing the convective heating rate there.

Conclusions

When the thermochemical state of the inviscid region is calculated accurately (vacuum ultraviolet absorption mechanisms are expanded to include all known bands of C_2 and C_3) and the effect of spallation is accounted for, the calculated surface recession of the Galileo probe in the stagnation region agrees fairly closely with the flight data. In particular, spalled particles provide blockage of the radiative heat flux reaching the wall.

Acknowledgment

The author thanks M. Ahmed of Lawrence Berkeley National Laboratory for his help in determining the absorption cross section for C3 in the vacuum ultraviolet wavelength range.

References

[1] Milos, F. S., "Galileo Probe Heat Shield Ablation Experiment," *Journal of Spacecraft and Rockets*, Vol. 34, No. 6, Nov.–Dec. 1997, pp. 705–713.
doi:10.2514/2.3293

[2] Moss, J. N., and Simmonds, A. L., "Galileo Probe Forebody Flowfield Predictions During Jupiter Entry," AIAA Paper 82-0874, June 1982.

[3] Matsuyama, S., Ohnish, N., Sasoh, A., and Sawada, K., "Numerical Simulation of Galileo Probe Entry Flowfield with Radiation and Ablation," *Journal of Thermophysics and Heat Transfer*, Vol. 19, No. 1, Jan.–Mar. 2005, pp. 28–35.
doi:10.2514/1.10264

[4] Leibowitz, L. P., "Measurement of the Structure of Ionizing Shock Wave in a Hydrogen-Helium Mixture," *Physics of Fluids*, Vol. 16, No. 1, Jan. 1973, pp. 59–68.
doi:10.1063/1.1694174

[5] Howe, J. T., "Hydrogen Ionization in the Shock Layer for Entry into the Outer Planets," *AIAA Journal*, Vol. 12, No. 6, June 1974, pp. 875–876.
doi:10.2514/3.49371

[6] Furudate, M., Jeung, I-S., and Matsuyama, S., "Nonequilibrium Calculation of Flowfield over Galileo Probe," AIAA Paper 2006-383, Jan. 2006.

[7] Park, C., "Dissociative Relaxation in Viscous Hypersonic Shock Layers," *AIAA Journal*, Vol. 2, No. 7, July 1964, pp. 1202–1207.
doi:10.2514/3.2522

[8] Park, C., "Injection-Induced Turbulence in Stagnation-Point Boundary Layers," *AIAA Journal*, Vol. 22, No. 2, Feb. 1984, pp. 219–225.
doi:10.2514/3.8371

[9] Perini, L. L., "Curve Fits of JANAF Thermochemical Data," Johns Hopkins Univ., Applied Physics Lab., Rept. ANSP M-5, Baltimore, MD, Sept. 1972.

[10] *NIST Atomic Spectra Database* [online database], Ver. 3, National Inst. of Standards and Technology, Gaithersburg, MD, http://physics.nist.gov/PhysRefData/ASD/index.html, Mar. 1995, [retrieved May 2009].

[11] Peach, G., "Continuous Absorption Coefficients for Non-Hydrogenic Atoms," *Memoirs of the Royal Astronomical Society*, Vol. 73, Pt. 1, 1970, pp. 1–123.

[12] Nicolas, C., Shu, J., Peterka, D. S., Hochlaf, M., Poisson, L., Leone, S. R., and Ahmed, M., "Vacuum Ultraviolet Photoionization of C3," *Journal of the American Chemical Society*, Vol. 128, No. 1, Jan. 2006, pp. 220–226.
doi:10.1021/ja055430+

[13] Pouilly, B., Robbe, J. M., Schamps, J., and Roueff, E., "Photodissociation and Radiative Processes in Interstellar C_1," *Journal of Physics B: Atomic and Molecular Physics*, Vol. 16, No. 3, 1983, pp. 437–448.
doi:10.1088/0022-3700/16/3/018

[14] Toffoli, D., and Lucchese, R. R., "Near Threshold Photoionization of the Ground and First Excited States of C_2," *Journal of Chemical Physics*, Vol. 120, No. 13, 2004, pp. 6010–6018.
doi:10.1063/1.1651477

[15] Bruna, P. J., and Grein, F., "Spectroscopy of the C_2 Molecule: Valence and Rydberg States in the 7–10 eV Region: An Ab Initio Study," *Canadian Journal of Physics*, Vol. 79, Nos. 2–3, 2001, pp. 653–671.
doi:10.1139/cjp-79-2-3-653

[16] Davies, C. B., and Park, C., "Trajectories of Solid Particles Spalled from a Carbonaceous Heat Shield," *Entry Vehicle Heating and Thermal Protection Systems: Space Shuttle, Solar Starprobe, Jupiter Galileo Probe*, Progress in Astronautics and Aeronautics, Vol. 85, edited by P. E. Bauer, and H. E. Collicott, AIAA, New York, 1983, pp. 472–495.

[17] Park, C., "Interaction of Spalled Particles with Shock Layer Flow," *Journal of Thermophysics and Heat Transfer*, Vol. 13, No. 4, Oct.–Dec. 1999, pp. 441–449.
doi:10.2514/2.6482

[18] Park, C., Raiche, G. A., II, and Driver, D. M., "Radiation of Spalled Particles in Shock Layers," *Journal of Thermophysics and Heat Transfer*, Vol. 18, No. 4, Oct.–Dec. 2004, pp. 519–526.
doi:10.2514/1.8098

[19] Lundell, J. H., "Spallation of the Galileo Probe Heat Shield," AIAA Paper 82-0852, June 1982.

[20] Wakefield, R. M., and Pitts, W. C., "Analysis of the Heat-Shield Experiment on the Pioneer-Venus Entry Probes," AIAA Paper 80-1494, July 1980.